



P398: SIXTH SEMESTER PROJECT

**Removing Thermal Component
from Infrared Region of Reflectance
Spectroscopy Data of Ceres**

July 12, 2021

Soumik Bhattacharyya

Roll No.- 1811155

***Supervisor:* Dr. Guneshwar Thangjam**

School of Physical Sciences
National Institute of Science Education and Research
Bhubaneswar

Abstract

The planetary reflectance data taken by a spectrometer is a mixture of data from planet's reflection and thermal emission. In the near-infrared region of the Visible and IR Imaging Spectrometer (VIR) of NASA's Dawn mission, the thermal component of Ceres is much higher than the reflection component. Removing the thermal component from reflectance spectroscopy data requires instrumental calibration, correction of artifacts, determination of emissivity and temperature of the surface etc. In this report, these factors have been discussed and a method of removal of thermal component of Ceres has been devised. The method and algorithm has been applied on two of the most important regions of Ceres: Ernutet and Haulani craters. The temperature maps of these regions have also been produced and validated with previous works on the regions.

Acknowledgements

I would like to express my gratitude to my project supervisor Dr. Guneshwar Thangjum, who has been supporting and encouraging me throughout the work. I would also like to thank Nikhil Keshav, who has been working on a similar project. I am also thankful to School of Physical Sciences for giving us an opportunity of working on a project of our interest.

The data used in this project is from VIR spectrometer, Dawn spacecraft, NASA. The VIR instrument was funded and coordinated by the Italian Space Agency (ASI) and built by Selex ES, with the scientific leadership of the Institute for Space Astrophysics and Planetology, Italian National Institute for Astrophysics, Italy. It is operated by the Institute for Space Astrophysics and Planetology, Rome, Italy.

Soumik Bhattacharyya
NISER, Bhubaneswar
July 12, 2021

Contents

1	Introduction	1
2	Theoretical Background	3
3	Data	9
3.1	VIR instrument	9
3.2	Orbital Phases	10
3.3	Limitations	12
4	Data Analysis	13
4.1	Artifacts removal	13
4.1.1	VIR Correction Factor	13
4.1.2	Recurring Negative Values	14
4.1.3	Odd-Even Band Effect	15
4.1.4	Spectral Spikes	17
4.1.5	Vertical Stripes in Image	19
4.2	Methodology for Reflectance Correction	20
4.2.1	Effect of using different approaches for emissivity	22
5	Results and Discussion	25
6	Future Plans	31
	Appendices	35
	References	35

Reflectance spectroscopy is the study of electromagnetic flux as a function of wavelengths that has been reflected from a surface. Over the years, it has been proved to be the most powerful and important remote-sensing technology for determining surface lithologic composition of other solar system bodies. With the advancements of technology, the spectral coverage of reflectance spectroscopy has also increased. However, the spectral range useful for analysis is only in the region where the flux of reflectance spectra is much higher than that of the planet's own emitted spectra. But the thermal emission component of a planetary body increases significantly in the Infrared region, following Planck's equation of Blackbody equation.

As a result of that, the spectral signature in that region and beyond can not be studied efficiently. For example, a standard spectra for Dawn/VIR data of Ceres has been shown in image 1.1. The only absorption feature which is visible in the figure where the thermal component is present is the absorption near $2.7 \mu m$. On the contrary, the absorptions near 3, 3.5 and $4 \mu m$ are evident in the thermally corrected one.

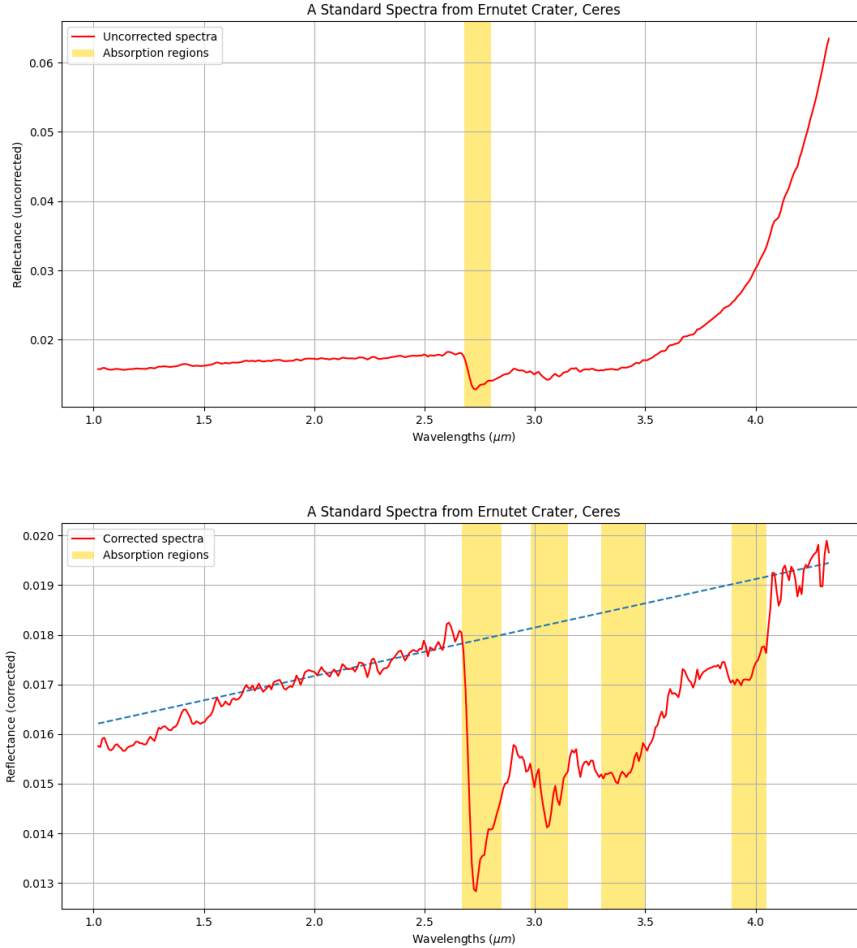


Figure 1.1: Comparison between a thermally corrected and uncorrected spectra of same location

In this report, a thermal correction algorithm has been developed and discussed for the Dawn/VIR spectrometer data of Ceres. The algorithm has been applied on the Ernutet and Haulani craters of Ceres. Corrected data cubes along with temperature maps of both the regions have been produced and discussed in this report.

Theoretical Background

When photons enter the surface of a planetary body, they are either scattered or absorbed by the medium. All natural surfaces above absolute zero temperature also emit photons through emission. In presence of atmosphere, the reflected or emitted photons may once again be scattered or emitted by atmosphere. However, in planetary bodies like Ceres, where there is no atmosphere, all the reflected or emitted spectra go back to space. Mathematically, the intensity flux received by a spacecraft spectrometer could be divided into two components, the intensity of reflected spectra and the intensity of emitted spectra.

$$I_{obs,\lambda} = I_{r,\lambda} + I_{t,\lambda} \quad (2.1)$$

where $I_{obs,\lambda}$ is the observed intensity by the spacecraft, $I_{r,\lambda}$ is the intensity of the reflectance spectra and $I_{t,\lambda}$ is the intensity of the thermally emitted spectra, all at wavelength λ .

Now, the definition of reflectance goes by the fraction of incident light scattered or reflected by a material. Although, depending upon the collimation of both source and detector, reflectance can be of different kinds. However, in reality all measured reflectances are biconical, where both the

source and detector are moderately collimated (Hapke, 2012). The formula for reflectance is given by,

$$R_\lambda = \frac{I_{r,\lambda}}{I_{i,\lambda}} \quad (2.2)$$

where R_λ is the reflectance at wavelength λ , $I_{r,\lambda}$ and $I_{i,\lambda}$ are respectively the intensities of reflected spectra and incident spectra at wavelength λ . Both $I_{r,\lambda}$ and $I_{i,\lambda}$ are given in $Wm^{-2}rad^{-1}$ per wavelength unit. Dividing equation 2.1 by $I_{i,\lambda}$ yields,

$$\begin{aligned} \frac{I_{obs,\lambda}}{I_{i,\lambda}} &= \frac{I_{r,\lambda}}{I_{i,\lambda}} + \frac{I_{t,\lambda}}{I_{i,\lambda}} \\ \Rightarrow R'_\lambda &= R_\lambda + \frac{I_{t,\lambda}}{I_{i,\lambda}} \end{aligned} \quad (2.3)$$

where R'_λ is the uncorrected reflectance with thermal component. $I_{i,\lambda}$ is calculated from the solar flux (F_{Sun}) data at 1 AU for each wavelength. Light Intensity is inversely proportional to the square of the distance. So, if F'_{Sun} is the solar flux received at the surface of Ceres and the distance between Sun and Ceres is d , then F'_{Sun} is given by,

$$F'_{Sun} = F_{Sun}/d^2 \quad (2.4)$$

Now, the relation between F_{Sun} and $I_{i,\lambda}$ is given by,

$$\begin{aligned} F'_{Sun} &= \int_0^\pi I_{i,\lambda} d\theta \\ &= \pi \cdot I_{i,\lambda} \\ \therefore I_{i,\lambda} &= \frac{F_{Sun}}{d^2 \times \pi} \end{aligned} \quad (2.5)$$

Putting equation 2.5 in equation 2.3,

$$R'_\lambda = R_\lambda + d^2 \times \frac{I_{t,\lambda} \times \pi}{F_{Sun}} \quad (2.6)$$

Now, the only unknown term in equation 2.6 is $I_{t,\lambda}$, which can be found from the Planck's equation for blackbody equation. According to which, the spectral radiance of a body at wavelength λ at absolute temperature T is given by,

$$U(\lambda, T) = \frac{2\pi hc^2}{\lambda^5} \frac{1}{e^{hc/\lambda k_B T} - 1} \quad (2.7)$$

where h is Planck's Constant, c is the speed of light and k_B is Boltzmann's constant. The quantities $c_1 = 2\pi hc^2 = 3.742 \times 10^{-16} W m^2$ and $c_2 = hc/k_B = 0.01439 mK$ are respectively called the first and second radiation constants. Now, blackbody is defined as an idealized physical body that absorbs all incident electromagnetic radiation of all wavelengths. However, no physical body can act as a perfect blackbody. To apply Planck's equation, the emissivity ($\epsilon(\lambda)$) value of the material must be multiplied with the Planck's equation. The spectral emissivity ($\epsilon(\lambda)$) is given by the actual power emitted by a surface ($U_a(\lambda, T)$) to that emitted by a blackbody (Hapke, 2012).

$$\epsilon(\lambda) = \frac{U_a(\lambda, T)}{U(\lambda, T)} \quad (2.8)$$

Although the value of emissivity depends on the wavelength, but it is not possible to find out emissivity for every wavelength value effectively unless we know any of the unknown parameters (temperature, reflectance value or lithologic composition). Also, it does not vary much in the working range. So,

for reflectance spectroscopy purposes, emissivity is often taken as a constant value and calculated from the Kirchhoff's law for Lambert surfaces (Clark, 1979),

$$\epsilon = 1 - R \quad (2.9)$$

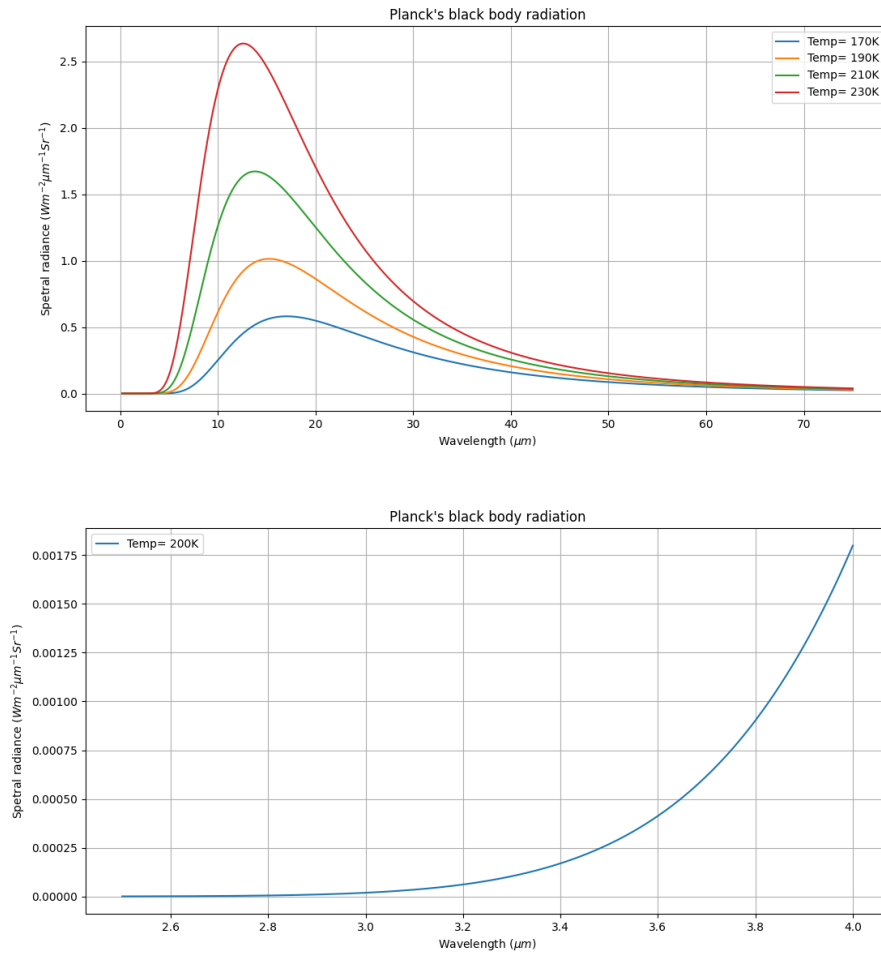


Figure 2.1: The increase in spectral radiance in near-infrared region in temperature range of Ceres is shown in the plot above. The second figure shows the increase in value in a stretched scale. This explains the sudden rise of uncorrected reflectance value in Image 1.1.

A detailed description for emissivity value taken in this project has been discussed in chapter 4. Putting emissivity and Planck's function in equation 2.6 gives us the final expression for reflectance (R).

$$\begin{aligned} R' &= R + d^2 \times \frac{\epsilon \times U(\lambda, T) \times \pi}{F_{Sun}} \\ \Rightarrow R &= R' - d^2 \times \frac{\epsilon \times U(\lambda, T) \times \pi}{F_{Sun}} \end{aligned} \quad (2.10)$$

where $U(\lambda, T)$ is given by equation 2.7.

Please note that the effect due to change in angle of incidence of solar flux has not been considered in formulation of 2.10 and it only holds for planets with no atmosphere.

Dwarf Planet Ceres, the largest object in the asteroid belt between Mars and Jupiter, was classified as an asteroid for a long time. In 2015, when Dawn went into orbit around Ceres, it became the first dwarf planet to be orbited by a spacecraft. Dawn is also the first spacecraft to orbit two extraterrestrial bodies (Vesta and Ceres).

3.1 VIR instrument

The Visible and IR imaging spectrometer (VIR) of Dawn has been built by the Italian Space Agency (ISA). It is a Shafer telescope combined with an Offner imaging spectrometer and images are formed on two matrix detectors—the VIS channel ($0.25\text{--}1.07\ \mu\text{m}$) and IR channel ($1.02\text{--}5.10\ \mu\text{m}$). As for temperature range in Ceres, the thermal component is considerable only in the IR range, so this work involves data from only the IR channel.

Table 3.1: Specifications on VIR infrared channel (Tosi et al., 2014)

Spectral range (nm)	1021-5098
Number of spectral channels	432
Average spectral sampling (nm/band)	9.46
Field of view ($^{\circ}\times^{\circ}$)	3.667×3.667
Field of view (mrad \times mrad)	64×64

The filter junctions of VIR-IR channel lies between $1.42\mu m < \lambda < 1.56\mu m$, $2.41\mu m < \lambda < 2.61\mu m$, $3.74\mu m < \lambda < 3.83\mu m$ and $4.35\mu m < \lambda < 4.54\mu m$ (Carrozzo et al., 2016). We need to be careful about using the data in those regions, which is marked in figure 4.1.

3.2 Orbital Phases

Depending upon the altitude of orbiter, the mission was divided into several phases: the Rotation Characterization 3 (RC3) phase, the Survey orbit phase, the High-Altitude Mapping Orbit (HAMO) phase, the Low-Altitude Mapping Orbit (LAMO) or Extended Mission Orbit 1 (XMO1) phase and other Extended Mission Orbit (XMO) phases.

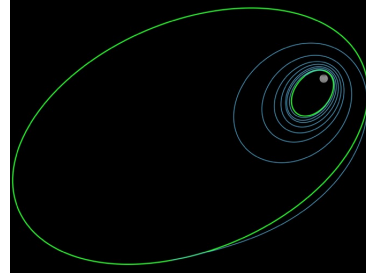


Figure 3.1: Dawn's orbits around Ceres [Image: NASA JPL]

From the table 3.2 and image 3.2, the difference in resolutions of images for different orbital phases can be observed. The RC3 data with a resolution 1.3 km/pixel has the worst resolution. The survey data was used in this project to develop the algorithm. Later, the algorithm was also applied on the HAMO data with required modifications. The LAMO data could be used in future for thermal correction and also for generating temperature map of the entire planet.

Table 3.2: A comparison between different phases of the orbital mission

Orbital Phase	Altitude (km)	Resolution (m/pixel)
RC3	13500	1300
Survey	4400	410
HAMO	1450	140
LAMO	375	35

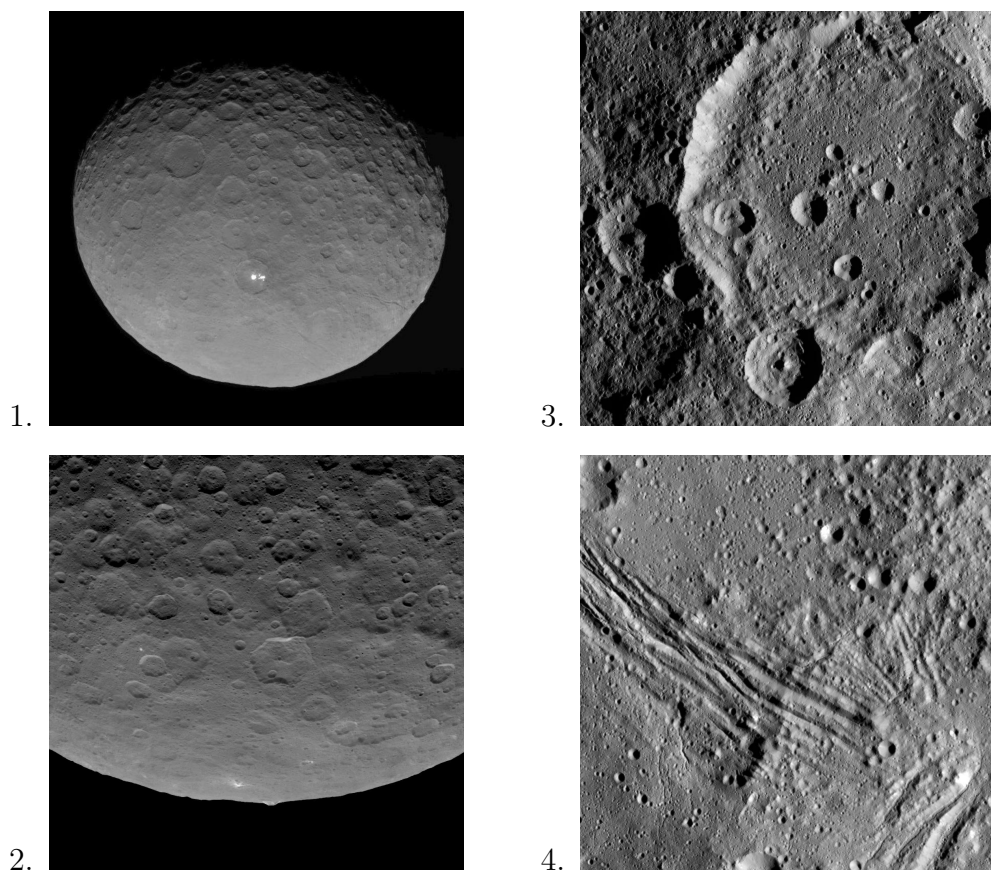


Figure 3.2: A contrast in the resolution of images taken in four different orbital phases (1. RC3, 2. Survey, 3.HAMO, 4.LAMO) can be observed here. [Image: NASA JPL]

3.3 Limitations

Except for a very few bright spots, Ceres has a very high value of emissivity (>0.95). So the reflectance data lies mostly in the range of 0-0.1 (following Kirchhoff's Law, equation 2.9). Physically, this indicates that the spectrometer instrument receives light of very less intensity. This leads to a lot of abnormalities/ artifacts in Data. Artifacts removal have been discussed in details in the next chapter.

Along with that, VIR has a sensitivity limited to $5\mu m$. This results in a lower limit of $180K$ for measuring temperature, that means no temperature below this can be safely measured without errors (Tosi et al., 2014). So, temperature of night-side of Ceres cannot be measured safely using VIR data.

Also, it is generally suggested by the VIR team not to use the data beyond $4\mu m$ or $4.33\mu m$.

4.1 Artifacts removal

As mentioned in previous section, the Dawn/VIR data in infrared channel contains several artifacts due to low intensity of light and instrumental errors.

4.1.1 VIR Correction Factor

Apart from the recurring systemic errors, a VIR correction factor is applied used on the VIR infrared data for calibration. It is provided by the VIR team of ISA and attached in Appendix A. Two plots without and with the VIR correction factor are shown in the figure below.

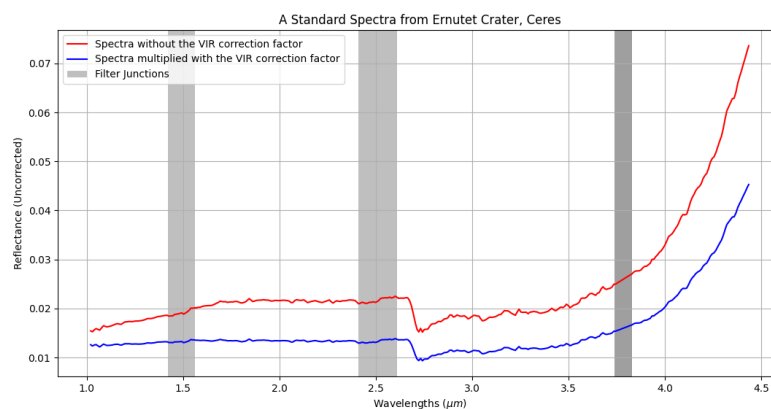


Figure 4.1: Spectra of same pixel from Survey data

4.1.2 Recurring Negative Values

One of the major errors is presence of negative values of order 10^{38} in data. This kind of error in data is solely due to instrumental errors and this is very systematic in nature.

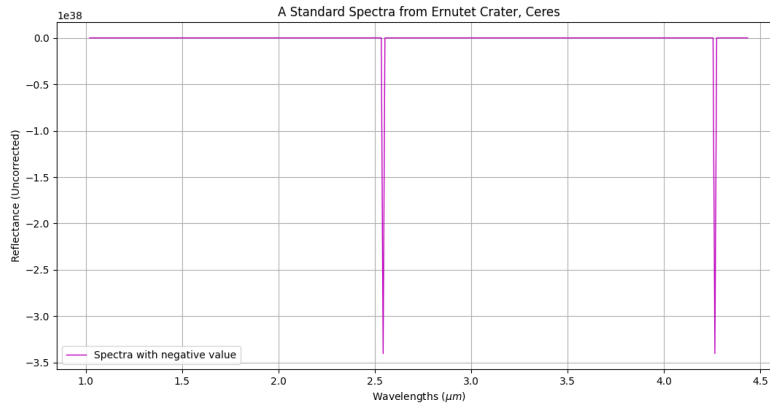


Figure 4.2: Presence of negative value in a few bands destroys the quality of the entire data

The following algorithm has been followed to remove these values.

1. If there are more than 10 bands with negative values present in same pixel, then the values for that pixel is rejected.
2. A pixel is also rejected if negative values are present in one or more bands in the main absorption region ($2.5\mu m < \lambda < 3.5\mu m$)
3. The rest of the values, identified as errors are then substituted with a polynomial of second degree fitting 5 neighbouring bands (Carrozzo et al., 2016).

Although, in Carrozzo et al. (2016), spikes are fitted with neighbouring 20 bands, but including so many number of bands for fitting one band value

increase the probability of including value from absorption region. Table 4.1 shows how this correction algorithm corrects the faulty data.

Wavelength (μm)	Data with Negative Error	Corrected Data
4.24638	0.032941	0.032941
4.25584	0.033866	0.033866
4.2653	-2.0939E+38	0.034317
4.27476	0.034936	0.034936
4.28421	0.035524	0.035524

Table 4.1: The negative value at 4.2653 μm is substituted with value using the algorithm above

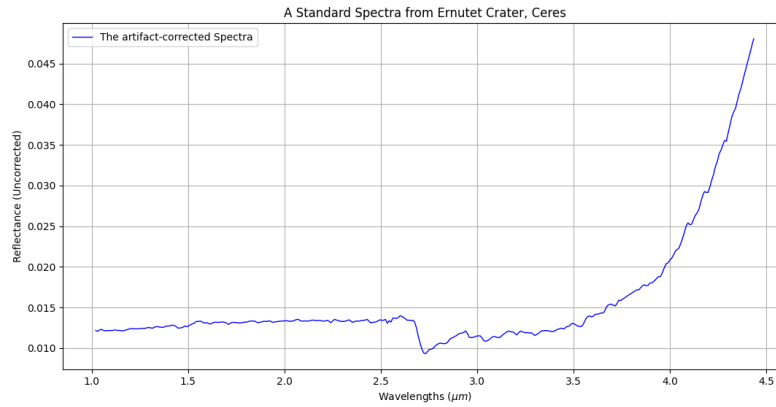


Figure 4.3: The same spectra as fig. 4.2 when negative errors are removed

4.1.3 Odd-Even Band Effect

A saw-tooth pattern in data is a common problem found in detectors. Minimizing this effect is also another task before going into thermal removal. Carrozzo et al. (2016) has also discussed this error in details. Figure 4.4 from Carrozzo et al. (2016) shows a typical Odd-Even Band effect in reflectance spectroscopy data.

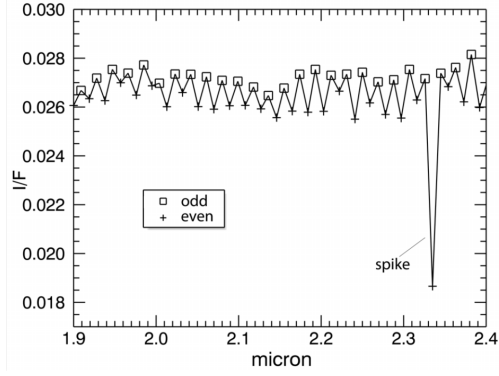


Figure 4.4: A typical Odd-Even Band effect in VIR-IR channel reflectance spectroscopy data of Ceres [Image: Carrozzo et al. (2016)]

The standard procedure to minimize this effect is by the means of interpolation. For every band data of even index, a weighted average is calculated from two of its neighbouring bands with odd index. Similar procedure is followed for data with odd index as well. So, now we have two sets of data for same pixel, one where all the odd-indexed band data is data from detector and the even-indexed band data is the weighted average data. The other data-set contains the exact opposite data, i.e. here all the even-indexed band data is data from detector. Finally, the minimized odd-even effect data is found by taking an average of values from both the data-sets for each wavelength.

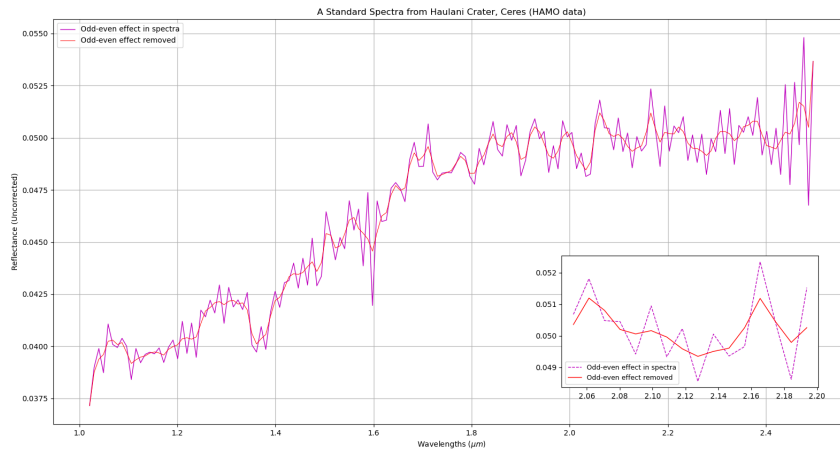


Figure 4.5: Data from a standard pixel after using the algorithm above

Fig. 4.5 is a typical example of Odd-Even effect on VIR-IR data. This is a standard spectra of Haulani Crater from HAMO phase of mission. As it can be seen from figure, this algorithm removes the effect as well as smooths the data.

4.1.4 Spectral Spikes

Spectral spikes are local anomalies found in data due to a large number of possible reasons, i.e. a cosmic ray hitting the detector. These kind of anomalies are usually found as a spike (or sometimes as a deep) in the data (see Fig. 4.4). These kinds of errors are easily recognisable in a single spectra, but for a large data, we need to find an efficient enough algorithm to find most of the spikes from data and rectify those. The most accepted model for detecting the spikes via statistical method is the $3\text{-}\sigma$ control limits, application of which has been discussed in Carrozzo et al. (2016).

- **Procedure:**

1. The data is in a three dimensional matrix format, i.e. for every pixel and wavelength, there is a corresponding row, sample (column) and band value data associated. For each sample, all the row data are selected from the Survey stage data.
2. For each sample, median value ($S_{med}(s, \lambda)$) of all row at each wavelength is calculated.
3. For each $S_{med}(s, \lambda)$, $3\text{-}\sigma$ threshold is applied for each wavelength to find out which of the rows have values outside the limit.

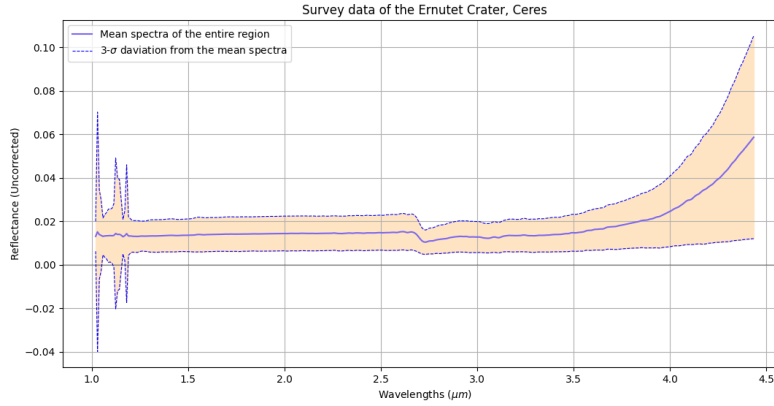


Figure 4.6: Mean spectra and $3\text{-}\sigma$ deviation of a randomly selected column has been shown here. Due to errors in VIR-IR channel, a high and random deviation can be observed in the region $1\mu m$ to $1.25\mu m$

- **Limitations:**

The spike detection algorithm has been applied on certain areas of Ceres. Different kind of anomalies have been found while doing that.

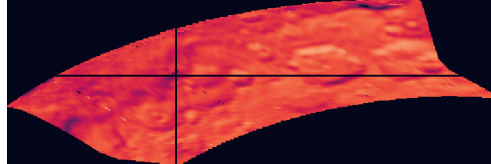


Figure 4.7: A location from Ernutet Crater Region, Ceres

The location shown in Fig. 4.7 is a darker region compared to other areas from the same column. The total intensity of light reflected from that pixel is very low compared to other regions. As a result of that the spectra of that entire region lies outside the $3\text{-}\sigma$ limit. Moreover, there is a spike at $1.26\mu m$, but that lies inside the limit (Fig. 4.8).

One of the possible solution to this problem could be accounting just a few neighbouring rows or checking the number of band values which are

outside the limit. However, that has not been included in this work.

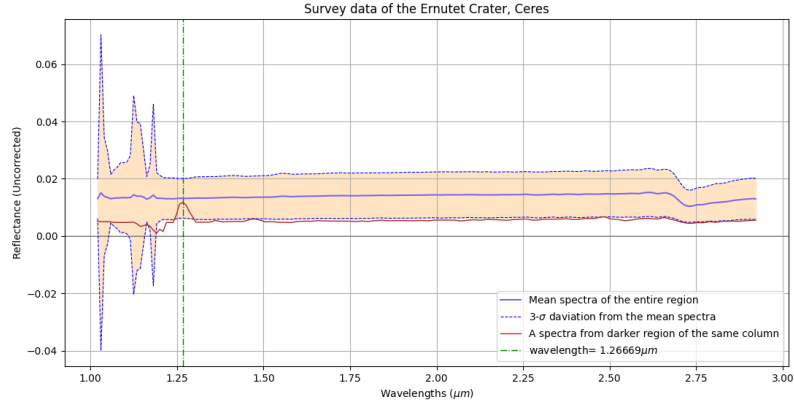


Figure 4.8: Spectra of a darker region lies outside the $3\text{-}\sigma$ limit despite having no spectral spike or deep. But the actual spikes in those regions fall inside the limit.

4.1.5 Vertical Stripes in Image

Presence of vertical stripes in data (fig. 4.9) is one among other artifacts. This should not be a concern for applying the reflectance correction algorithm on smaller area. However, this should be rectified while applying the algorithm on a bigger area.

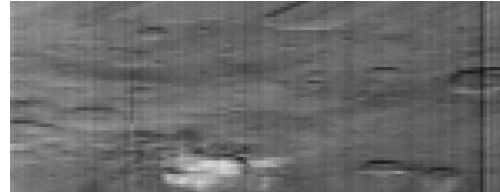


Figure 4.9: Vertical Stripes in VIR-IR data

4.2 Methodology for Reflectance Correction

After artifact correction, we move forward to Reflectance Correction. The methodology of which broadly follows from Clark et al. (2011) and Bandfield et al. (2018). However, both of the papers are for lunar data and certain changes had to be applied to use the methodology for Dawn/VIR data of Ceres.

1. For each spectrum, reflectance is linearly fitted in the non-absorption region ($1.7\mu m$ to $2.41\mu m$) and projected to the entire spectra ($1 - 4.33\mu m$). Although, Ceres does not show any absorption feature in the region $1 - 2.6\mu m$, there are certain reasons that the entire region is not used for the straight line fitting. Firstly, data in $1 - 1.2\mu m$ is largely affected by instrumental error (Fig. 4.6). Also, a difference in slope between the regions $1 - 1.7\mu m$ and $1.7 - 2.6\mu m$ is observed. The VIR correction factor minimizes the difference, but it is still present in most of the spectra. The region $2.41\mu m$ to $2.61\mu m$ is neglected because it falls in a filter junction.

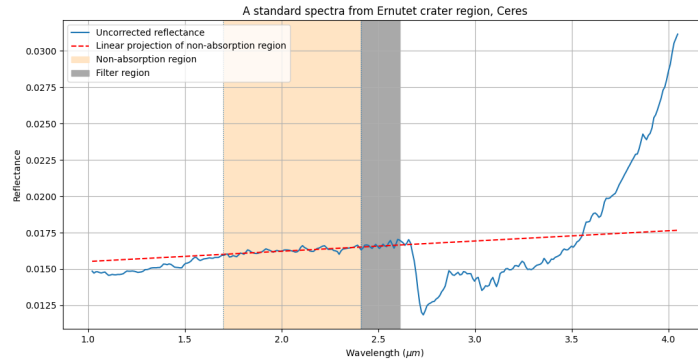


Figure 4.10: Linear projection from non-absorption region to entire spectra (only till $4.04\mu m$ is shown in figure)

2. Now, the projected reflectance value is subtracted from the uncorrected spectra to find the apparent thermal component for the entire wavelength region mixed.
3. This thermal component list is then compared to the actual thermal component, which is given by $d^2 \times \frac{\epsilon \times U(\lambda, T) \times \pi}{F_{Sun}}$ (from equation 2.10) for each wavelength. The unknown factors in this equation are distance from Sun to Ceres (d), emissivity (ϵ) and temperature (T).
4. **Distance from Sun to Ceres:** The distance from Sun to Ceres varies during the entire mission. For example, the distance while taking the Survey data should be different from the distance while taking the HAMO data. In this project the average distance between Sun and Ceres (2.8 AU) has been used. However, to use the algorithm over a broader region, the exact distance should be used for every column of data.
5. **Emissivity:** The emissivity value has been calculated from Kirchhoff's Law for lambert surfaces (equation 2.9), i.e. $\epsilon = 1 - r$, where r is mean reflectance of the non-absorption region. Effect of using different approaches for determining emissivity has been discussed later in this section.
6. The apparent thermal emission list is now fitted for temperature with the formula $d^2 \times \frac{\epsilon \times U(\lambda, T) \times \pi}{F_{Sun}}$ in such a way that it deviates least in the range ($4.1\mu m$ to $4.33\mu m$), i.e. the range where the absorption near 3.9 ends till the entire effective region.
7. The actual thermal component is calculated using the formula and it is

subtracted from the uncorrected data to get the corrected reflectance spectra.

4.2.1 Effect of using different approaches for emissivity

As discussed in section 2, the emissivity value for a planetary body is often taken as a constant value and calculated using Kirchhoff's law (equation 2.9). For Ceres, the most commonly used emissivity values are either 0.9 or 0.95. In this section, comparison has been drawn between several approaches of finding emissivity.

1. Emissivity as a function of wavelength:

In this approach, emissivity value has been calculated for each wavelength using the Kirchhoff's Law. First, a linear projection has been made from the non-absorption region to the entire region. Now, for each wavelength emissivity has been calculated by using the following relation,

$$e(\lambda) = 1 - r(\lambda)$$

where $r(\lambda)$ is value of the extended straight line at wavelength λ . This method has been applied on the Survey data from Ernutet crater region. The mode of the emissivity values, calculated from this method, has been found to be at 0.985.

2. Emissivity from mean reflectance of non-absorption region:

In this method, emissivity is calculated for the entire wavelength region

from the mean reflectance of the non-absorption region.

$$e = 1 - r_{mean}$$

This method is also applied on the same data and the mode of emissivity values has been found to be at 0.983.

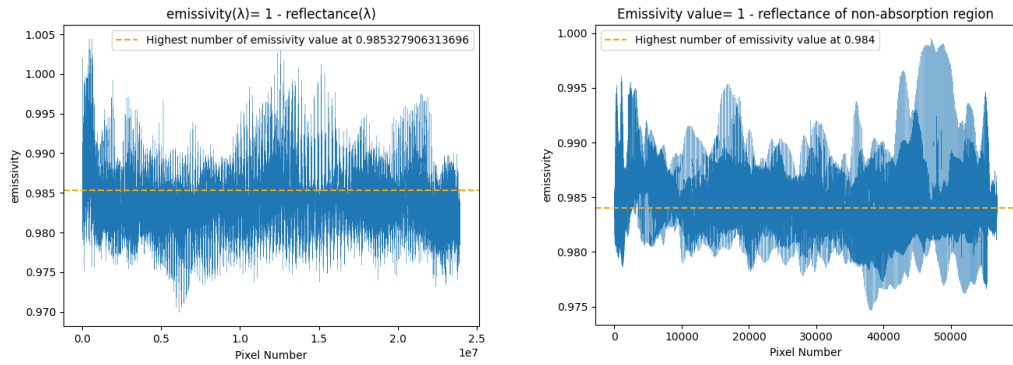


Figure 4.11: Distribution of emissivity values on Ernutet crater region by Method 1 (left) and Method2 (right)

3. Emissivity as constant value:

Here, emissivity has been taken as a constant value (0.95) like most other works on Ceres. A temperature map has been produced using each method for comparison.

- **Effect on Temperature:**

A temperature map has been generated using all three approaches. As it can be observed from figure 4.12, the change in emissivity values in such small range does not affect the temperature much. However, it is important to choose the most appropriate method. The main reason behind rejecting

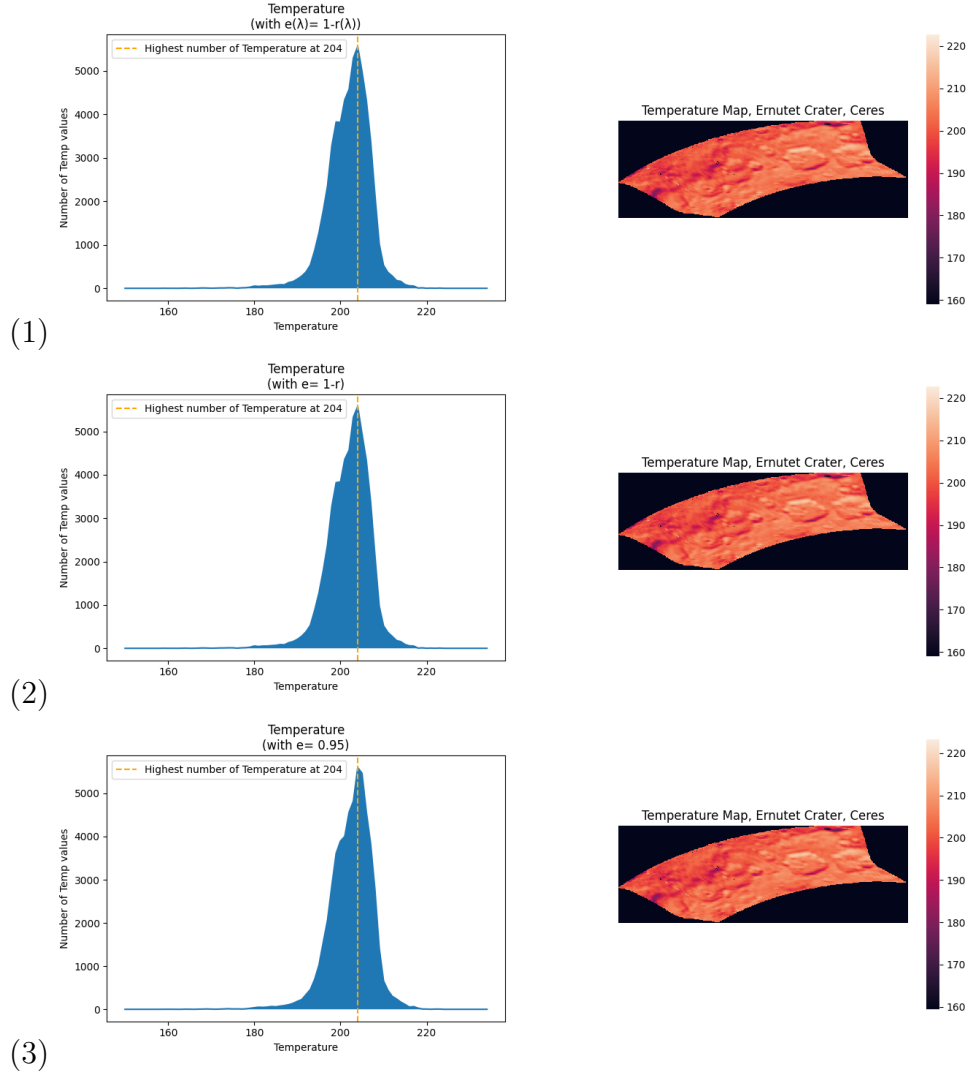


Figure 4.12: Distribution of temperature and temperature map of Ernutet crater region by Method 1, Method 2 and Method 3

the first method is, sometimes it gives emissivity value greater than one near $1\mu m$, which is physically impossible. Although the third method was applied in Tosi et al. (2018), it was focused only on Haulani crater, which shows relatively higher value of reflectance, thus making this approach suitable. However, it may not be applicable on darker regions of Ceres.

Results and Discussion

The methodology of thermal correction has been applied on Ernutet and Haulani crater region of Ceres. Both of these regions have recently gained the attention of geoscientific community for different reasons. The Ernutet crater region has shown proof of existence of organic molecules (Kaplan et al., 2018), while temperature anomalies have been found in Haulani (Tosi et al., 2018).

For Ernutet region, the algorithm has been applied both on survey and HAMO data, while only HAMO data has been used for Haulani region. The data, artifact corrected version of data (only those artifacts which are discussed in this report) and reflectance corrected file has been added in this *google drive folder* (in case it doesn't work, please copy and paste this url: https://drive.google.com/drive/folders/1H_ej6ewChWTYJMtfKFS6IZaz0fAVk10t?usp=sharing).

Along with that, best fitted temperature for each pixel has been recorded and plotted as a temperature map.

1. Ernutet Crater

A well fitted standard spectrum from Ernutet region (Survey data)

looks like figure 5.4. The corrected reflectance has been brought down to the level of linear projection of non-absorption region. Another spectra from the same region has been plotted from HAMO data (5.2). Except for some instrumental errors, both the spectrum shows similar pattern. The recorded temperature for these two pixels are respectively 211.04K and 221.20K, both of which are within range of daytime temperature of Ceres.

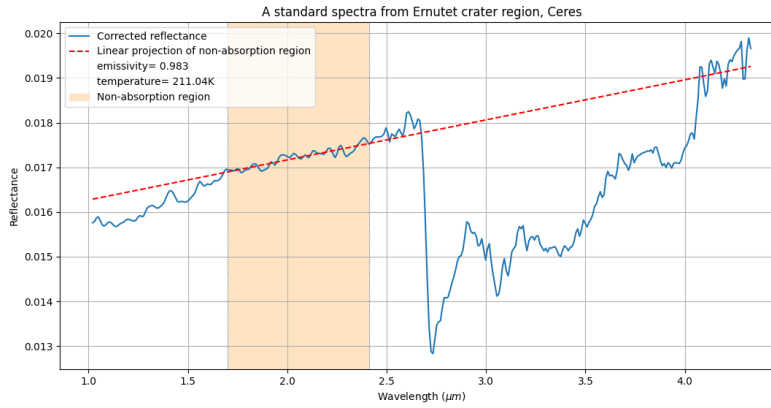


Figure 5.1: A standard corrected spectrum from Ernutet region, survey data

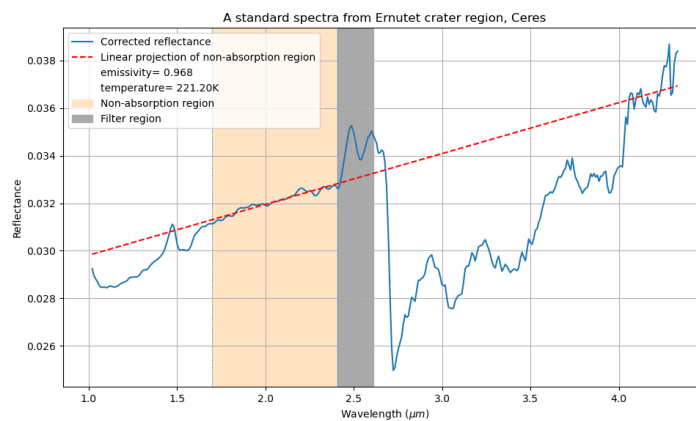


Figure 5.2: A standard corrected spectrum from Ernutet region, HAMO data

Temperature map for both the regions have been plotted and it is shown below. All the temperature value mentioned in figure 5.3 and ?? are in Kelvin.

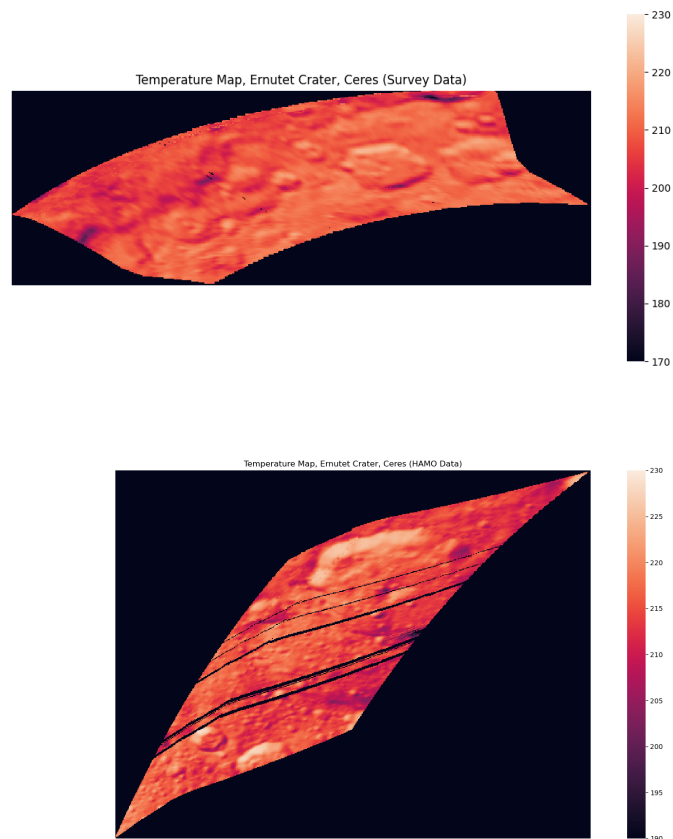


Figure 5.3: Surface temperature map of Ernutet region obtained respectively from survey data and HAMO data. The map has been plotted in a "dark red" scale, where the low temperature regions are shown in a darker shade and the higher temperature region is shown in a whiter shade.

As it can be observed, the topographical effect is visible in both the maps, which should be removed in the next step of the work before going to spectral analysis.

2. Haulani Crater

A standard spectra from Haulani crater, corrected from HAMO data can be observed in the figure below.

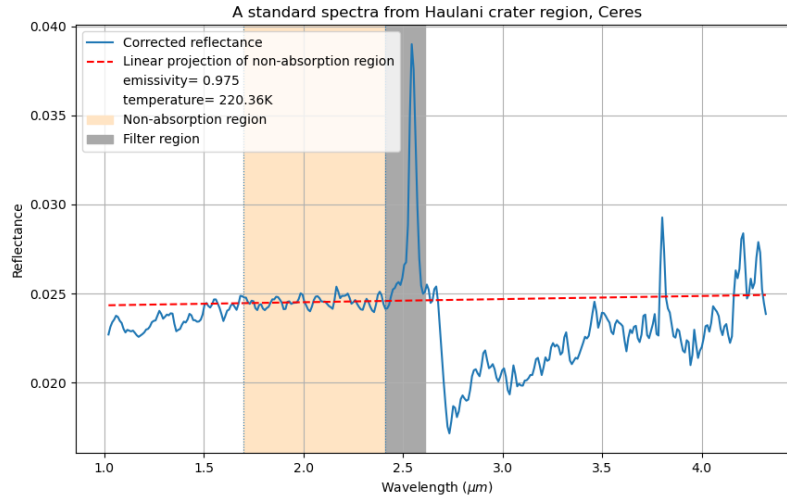


Figure 5.4: A standard corrected spectrum from Haulani region, survey data

The HAMO data of Haulani crater shows more artifacts than the Ernutet region. In most of the pixels, a spike has been observed in the filter region

2.41 μm to 2.61 μm . It also shows

slightly different features from the spectra from Ernutet region, the main reason being presence of organic molecules in the later area.

The spectra can be matched with figure 5.5, which

is a mean spectra from the same region, as published in Tosi et al. (2018).

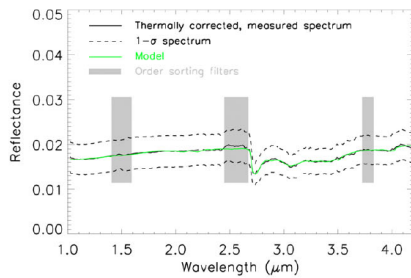


Figure 5.5: Mean spectra from certain region of Haulani region has been plotted in Tosi et al. (2018).

First temperature anomalies of Ceres were observed in Haulani crater data of approach phase of the mission. This region showed a distinct thermal contrast, being $\sim 5K$ cooler than the rest of the surface (Tosi et al., 2015). The temperature map plotted in this algorithm is compared with that of Tosi et al. (2018) in figure 5.6 and 5.7.

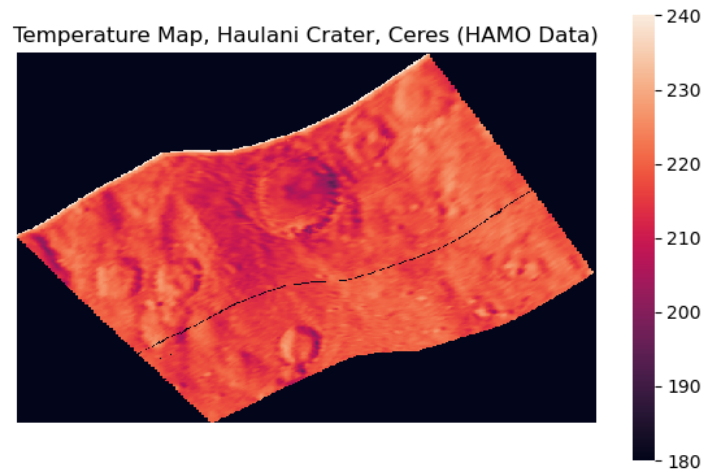


Figure 5.6: Surface temperature map of Ernutet region obtained respectively from survey data and HAMO data. The map has been plotted in a "dark red" scale, where the low temperature regions are shown in a darker shade and the higher temperature region is shown in a whiter shade.

In this map, it can be observed that the central region of Haulani shows darker shades, which indicates the low temperature of the region. Those regions have a relatively higher value of reflectance and less value of emissivity. These lower temperature regions could be located in Tosi et al. (2018) as well. Both of the maps also lie in same temperature range, which validates the result.

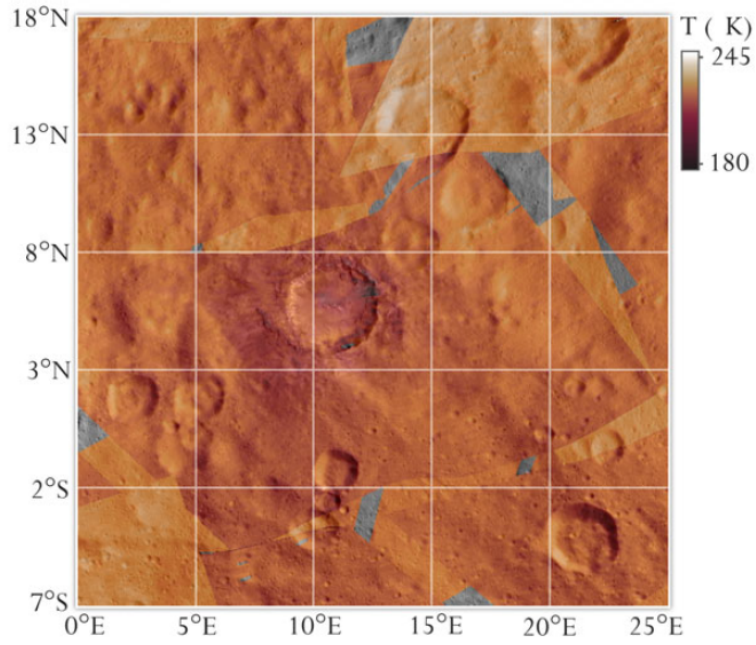


Figure 5.7: This surface temperature map of Haulani region from Tosi et al. (2018) shows similarities with the temperature map which is plotted using our methodology.

Future Plans

The main reason behind thermal correction of reflectance spectroscopy data is to make the spectra suitable for spectral analysis, which is also the main motif behind this project. But before that, there are several other steps and corrections which have to be implied.

Firstly, artifacts corrections should be given more importance. for example, as it was mentioned in section 4, detection algorithm for spectral spikes should be improved for applying on darker and brighter regions. Distance between Sun and Earth is also to be updated according to distance of taking images. Following these corrections, this algorithm can be applied on bigger surface areas, eg. the entire planet, for reflectance correction and generating the temperature map.

As it can be seen from figure ??, the topography of the area can be visible in the temperature map. This brings us to the next step of the project, that is the topographical corrections and the angle of incident correction. Following all these corrections, the data may be finally used for spectral analysis.

Appendices

References

- Joshua L. Bandfield, Michael J. Poston, Rachel L. Klima, and Christopher S. Edwards. Widespread distribution of oh/h₂o on the lunar surface inferred from spectral data. *Nature Geoscience*, 11, 2018. doi: <https://doi.org/10.1038/s41561-018-0065-0>.
- F. G. Carrozzo, A. Raponi, M. C. De Sanctis, E. Ammannito, M. Giardino, E. DAversa, S. Fonte, and F. Tosi. Artifacts reduction in vir/dawn data. *Review of Scientific Instruments*, 87, 2016. doi: <https://doi.org/10.1063/1.4972256>.
- Roger N. Clark. Planetary reflectance measurements in the region of planetary thermal emission. *Icarus*, 40, 94-103, 1979. doi: [https://doi.org/10.1016/0019-1035\(79\)90056-3](https://doi.org/10.1016/0019-1035(79)90056-3).
- Roger N. Clark, Carl M. Pieters, Robert O. Green, J. W. Boardman, and Noah E. Petro. Thermal removal from nearinfrared imaging spectroscopy data of the moon. *Journal of Geophysical Research*, 116(E00G16), 2011. doi: <https://doi.org/10.1029/2010JE003751>.
- Bruce Hapke. *Theory of Reflectance and Emittance spectroscopy*. Cambridge University Press, 2nd edition, 2012.
- Hannah H. Kaplan, Ralph E. Milliken, and Conel M. OD. Alexander. New constraints on the abundance and composition of organic matter on ceres. *Geophysical Research Letters*, 45:52745282, 2018. doi: <https://doi.org/10.1029/2018GL077913>.
- F. Tosi, M.T. Capria, M.C. De Sanctis, J.-Ph. Combe, F. Zambon, A. Nathues, S.E. Schrder, J.-Y. Li, E. Palomba, A. Longobardo, D.T. Blewett, B.W. Denevi, E. Palmer, F. Capaccioni, E. Ammannito, T.M. Titus, D.W. Mittlefehldt, J.M. Sunshine, C.T. Russell, C.A. Raymond,

- and the Dawn/VIR Team. Thermal measurements of dark and bright surface features on vesta as derived from dawn/vir. *Icarus*, 240, 36-57, 11, 2014. doi: <http://dx.doi.org/10.1016/j.icarus.2014.03.017>.
- F. Tosi, De Sanctis M. C., Zambon F., Ammannito E., Capria M. T., Carrozzo F. G., Li J.-Y., Longobardo A., Mottola S., Palomba E., Raponi A., Raymond C. A., and Russell C. T. Preliminary temperature maps of dwarf planet ceres as derived by dawn/vir. *European Planetary Science Congress*, 2015.
- F. Tosi, F. G. Carrozzo, A. Raponi, M. C. De Sanctis, G. Thangjam, F. Zambon, M. Ciarniello¹, A. Nathues², M. T. Capria¹, E. Rognini¹, E. Ammannito, M. Hoffmann, K. Krohn, A. Longobardo, E. Palomba, C. M. Pieters, K. Stephan, C. A. Raymond, , and C. T. Russell. Mineralogy and temperature of crater haulani on ceres. *Meteoritics Planetary Science*, 53, 2018. doi: <https://doi.org/10.1111/maps.13078>.